Acta Mechanica 76, 161—187 (1989)

ACTA MECHANICA

Viscoplastic Behaviour of Stainless Steels AISI 316L and 316H

By

A. G. Youtsos, J. Donea, and **G. Verzeletti,** Ispra, Italy

With 21 Figures

(*Received October 12, 1987; revised November 26, 1987*)

Summary

The theory of viscoplasticity based on total strain and overstress is used in order to simulate the sensitivity to the rate of loading of two commonly used stainless steels, namely AISI 316L and 316H. The constitutive model has been implemented within a transient finite element computer code using a stress update algorithm based on the elastic predictor-return mapping concept. Both monotonic and cyclic loading conditions are considered in one or more space dimensions.

Experimental results showing strain-rate dependence at room temperature are reported for both types of steel and used for calibrating the viscoplastic numerical model. An explicit dependence of the nonlinear viscosity function on the strain rate has been obtained and the calibrated model is found to yield results which are in excellent agreement with the experimental data.

Finally the calibrated viscoplastic model is applied to predict the response of two representative structures subjected to impulsive loading. The results indicate a significant effect of the rate of loading on the internal stress distribution.

1. Introduction

The sensitivity to the rate of loading of commonly used stainless steels (e.g. AISI types 316L and 316H) has been the subject of many experimental investigations. These have revealed that stainless steels exhibit viscoplastic behaviour even at room temperature, their inelastic deformation being basically rate dependent. For example, experiments in monotonic loading performed at JRC-Ispra by Albertini et al. on 316H [1] and on 316L (reported herein) show that stress-strain curves for the above steels obtained at strain rates ranging from 10^{-4} to 10 s^{-1} for 316L and from 10^{-3} to 10^{3} s^{-1} for 316H exhibit a stress level difference of the order of 40% to 60%, respectively.

Various models have been proposed in the literature to describe rate-dependent

steel deformation behaviour. Among these the best known are probably those of Malvern [2], Perzyna [3], Bodner and Parton [4] and Cernocky and Krempl [5].

The constitutive theory used herein to model rate sensitivity is the theory of viscoplasticity based on total strain and overstress developed by Cernocky and Krempl [5]. This theory and its main properties are briefly recalled in Section 2. In Section 3 numerical techniques are proposed that allow for a systematic treatment of the chosen viscoplastic model in the context of transient finite element analysis. In particular a stress update algorithm is suggested which falls within the category of elastic predictor-return mapping algorithms widely used in computational plasticity.

In Section 4 experimental stress-strain — strain rate results are presented for stainless steel types 316L and 316H. Based on these experimental data, the parameters in the nonlinear viscosity function are obtained in Section 5 using a curve fitting procedure. Finally, using the calibrated viscoplastic model, numerical examples are presented in Section 6 which illustrate the significant effect of the rate of loading on the internal stress distribution.

2. Constitutive Theory

The theory of viscoplasticity based on total strain and overstress developed by Cernocky and Krempl [5] does not utilize the concept of a yield surface. The transition from linear elastic to nonlinear inelastic behaviour is smooth. A viscosity function and an equilibrium stress-strain diagram are used to characterize a material in monotonic loading.

2.1 Isotropic Constitutive Equation

Let σ_{ij} and ε_{ij} be the stress and strain tensors, respectively, for small deformations and let a superposed dot designate the time derivative. The isotropic constitutive equation proposed in [5] is

$$D_{ijkl}\dot{\varepsilon}_{kj} - \dot{\sigma}_{ij} = \frac{\sigma_{ij} - G_{ij}[\varepsilon_{kl}]}{\eta[\Gamma]} \tag{2.1}$$

where

$$D_{ijkl} = \frac{E}{1+\nu}\left[\frac{1}{2}\left(\delta_{ik}\delta_{jl} + \delta_{il}\delta_{jk}\right) + \frac{\nu}{1-2\nu}\,\delta_{ij}\delta_{kl}\right], \tag{2.2}$$

$$G_{ij} = \frac{g[\phi]}{E\phi}\, D_{ijkl}\varepsilon_{kl}, \tag{2.3}$$

$$\Gamma = [(\sigma_{ij} - G_{ij})\,(\sigma_{ij} - G_{ij})]^{1/2}, \tag{2.4}$$

$$\phi = \frac{1}{1+\nu}\left[\frac{3}{2}\, e_{ij}e_{ij}\right]^{1/2}, \tag{2.5}$$

$$e_{ij} = \varepsilon_{ij} - \frac{1}{3}\,\varepsilon_{kk}\delta_{ij}. \tag{2.6}$$

E is the elastic modulus and ν Poisson's ratio. The function $\boldsymbol{G}$ is the equilibrium stress-strain curve and reduces to the uniaxial equilibrium stress-strain curve $g[\varepsilon]$ when the uniaxial state of strain is substituted in (2.3). The quantity Γ in (2.4) is the overstress magnitude; ϕ in (2.5) is the usual effective strain and $\boldsymbol{e}$ in (2.6) is the deviatoric strain tensor. The viscosity function $\eta[\Gamma]$, dimension time, is positive, continuous and bounded; further it is required that $d\eta[\Gamma]/d\Gamma < 0$. Note that the constitutive Eq. (2.1) is linear in the stress-rate and the strain-rate tensors but non-linear in the stress and the strain tensors.

2.2 Properties of Constitutive Theory

As illustrated in [5] the constitutive theory described by (2.1) is endowed with many desirable properties. For fast loading conditions, which are of interest herein, the interesting properties of (2.1) are:

— Initial linear elastic behaviour;
— Initial elastic slope upon large instantaneous changes in strain rate in the plastic region under any state of stress;
— Strain (stress) rate sensitivity of the stress-strain curves;
— Defined behaviour in the limit of very slow and very fast loading rates;
— Stress-strain curves obtained at different constant strain rates will ultimately have the same slope;
— Highly non-linear spacing of the stress-strain diagrams due to the dependence of the viscosity function η upon the overstress magnitude Γ.

3. Numerical Formulation

In this section, numerical techniques are proposed that allow for a systematic treatment of the visco-plastic constitutive model discussed in Section 2 within the context of finite element transient analysis.

The stress update algorithm which is suggested here is adapted from an algorithm for linear viscosity (η = constant) described in a recent paper by Simo and Ortiz [6]. This algorithm falls within the category of elastic predictor-return mapping algorithms widely used in computational plasticity (see, e.g. the excellent review by Hughes [7]).

3.1 Elastic-Viscoplastic Operator Split

We start by rephrasing the visco-plastic constitutive Eq. (2.1) so as to give it a structure reminiscent of constitutive equations for inviscid plasticity. Using direct notation we rewrite (2.1) as

$$\dot{\boldsymbol{\sigma}} = \boldsymbol{D} \cdot \dot{\boldsymbol{\varepsilon}} - \frac{1}{\eta} \boldsymbol{Z} \tag{3.1}$$

where $\boldsymbol{Z} = \boldsymbol{\sigma} - \boldsymbol{G}$ is the overstress. From the definition (2.4) of the overstress magnitude Γ, it is observed that

$$\frac{d\Gamma}{d\boldsymbol{Z}} = \frac{\boldsymbol{Z}}{\Gamma} \tag{3.2}$$

and

$$\left\| \frac{d\Gamma}{d\boldsymbol{Z}} \right\| = 1. \tag{3.3}$$

Therefore, combination of (3.1) and (3.2) yields

$$\dot{\boldsymbol{\sigma}} = \boldsymbol{D} \cdot \dot{\boldsymbol{\varepsilon}} - \frac{\Gamma}{\eta} \frac{d\Gamma}{d\boldsymbol{Z}} \tag{3.4.1}$$

or, equivalently

$$\dot{\boldsymbol{\sigma}} = \boldsymbol{D} \cdot \left(\dot{\boldsymbol{\varepsilon}} - \frac{\Gamma}{\eta} \boldsymbol{D}^{-1} \frac{d\Gamma}{d\boldsymbol{Z}} \right) = \boldsymbol{D} \left(\dot{\boldsymbol{\varepsilon}} - \dot{\boldsymbol{\varepsilon}}^{vp} \right). \tag{3.4.2}$$

It is now apparent that the constitutive relation (3.4) is in a form similar to constitutive equations for inviscid plasticity, namely

$$\dot{\boldsymbol{\sigma}} = \boldsymbol{D} \cdot (\dot{\boldsymbol{\varepsilon}} - \dot{\boldsymbol{\varepsilon}}^{p}); \qquad \dot{\boldsymbol{\varepsilon}}^{p} = \dot{\Lambda} \boldsymbol{r} \tag{3.5}$$

where $\boldsymbol{r}$ indicates the plastic flow direction and $\dot{\Lambda}$ is the plastic rate parameter defined by the consistency condition. For an associated flow rule, $\boldsymbol{r}$ represents the unit outward normal to the yield surface. In particular, the constitutive relation (3.4) can be "split" into elastic and visco-plastic parts as required for applying return mapping algorithms.

The *elastic part* is deformation driven and is given by

$$\dot{\boldsymbol{\varepsilon}} = \dot{\boldsymbol{\varepsilon}}^{e} + \dot{\boldsymbol{\varepsilon}}^{vp} = \hat{\dot{\boldsymbol{\varepsilon}}}(t), \text{ (prescribed rate of total strain)}$$

$$\dot{\boldsymbol{\sigma}} = \boldsymbol{D} \cdot \dot{\boldsymbol{\varepsilon}}, \tag{3.6}$$

$$\dot{\boldsymbol{\varepsilon}}^{vp} = \boldsymbol{0}.$$

On the other hand, the *visco-plastic part* of the constitutive relation (3.4) reduces to

$$\dot{\boldsymbol{\varepsilon}} = \boldsymbol{0}; \quad \dot{\boldsymbol{\sigma}} = -\frac{\Gamma}{\eta} \frac{d\Gamma}{d\boldsymbol{Z}}. \tag{3.7}$$

Equation (3.7) defines a relaxation process for the stresses with a return path defined by $d\Gamma/d\boldsymbol{Z}$.

3.2 Rate of Change of Γ/η

The rate of change of Γ/η in (3.7) is given by

$$(\Gamma/\eta)^{\cdot} = \dot{\Gamma}/\eta - \Gamma\dot{\eta}/\eta^2 = \dot{\Gamma}/\eta - \Gamma \frac{\partial \eta}{\partial \Gamma} \dot{\Gamma}/\eta^2. \tag{3.8}$$

From the definition (2.4) of the overstress magnitude Γ one obtains

$$\dot{\Gamma} = \frac{\partial \Gamma}{\partial Z_{ij}} \dot{Z}_{ij} = \frac{Z_{ij}\dot{Z}_{ij}}{\Gamma}. \tag{3.9}$$

As indicated by (3.7) during the visco-plastic relaxation phase one has

$$\dot{\boldsymbol{\varepsilon}} = \mathbf{0} \tag{3.10}$$

and consequently

$$\dot{\boldsymbol{G}} = 0. \tag{3.11}$$

It then follows that

$$\dot{\boldsymbol{Z}} = \dot{\boldsymbol{\sigma}} = -\frac{\Gamma}{\eta} \frac{d\Gamma}{d\boldsymbol{Z}} = -\boldsymbol{Z}/\eta \tag{3.12}$$

so that the rate of change (3.9) of the overstress magnitude can be written as

$$\dot{\Gamma} = -\frac{Z_{ij}Z_{ij}}{\eta\Gamma} = -\Gamma/\eta. \tag{3.13}$$

Introducing (3.13) into (3.8) one finds that the rate of change of Γ/η is governed by the following equation

$$(\Gamma/\eta)^{\cdot} = -\Gamma/\eta \left(\frac{1 - \Gamma/\eta \dfrac{\partial \eta}{\partial \Gamma}}{\eta} \right) \tag{3.14}$$

which is the viscous counterpart of the consistency condition of inviscid plasticity. Defining an *instantaneous relaxation time* by the expression

$$\bar{t} = \frac{\eta}{1 - \dfrac{\partial \eta}{\partial \Gamma} \Gamma/\eta}. \tag{3.15}$$

(3.14) may be rewritten as

$$(\Gamma/\eta)^{\cdot} = -\frac{\Gamma/\eta}{\bar{t}}. \tag{3.16}$$

3.3 Stress Update: Return Mapping Algorithm

Based on the elastic-viscoplastic split (3.6), (3.7), a return algorithm can be defined by first solving the elastic Eq. (3.6) to obtain an elastic predictor, which is then taken as an initial condition for the visco-plastic relaxation Eq. (3.7).

As in inviscid plasticity, the return path for stresses is defined iteratively and comprises a sequence of straight segments. To compute the final location of the stress point in the return path, one may proceed as suggested by Simo and Ortiz [6].

(a) Within a generic straight segment (i) in the return path, the relaxation time is taken to be constant and equal to a value $\bar{t}^{(i)}$ computed according to (3.15) from the initial conditions, $\sigma_{n+1}^{(i)}$, for the segment, where subscript n indicates the time level.

(b) Thus, within a typical straight segment, the variation of Γ/η is given from (3.16) by the exponential relation

$$\Gamma/\eta = (\Gamma/\eta)_{n+1}^{(i)} \exp(-\Delta t/\bar{t}^{(i)}) \tag{3.17}$$

where Δt is the time elapsed since the entrance of the stress point into segment (i).

(c) The total time $\Delta t^{(i)}$ spent by the stress point in segment (i) is, therefore, given by

$$\Delta t^{(i)} = \bar{t}^{(i)} \log \frac{(\Gamma/\eta)_{n+1}^{(i)}}{(\Gamma/\eta)_{n+1}^{(i+1)}} \tag{3.18}$$

(d) The end of the relaxation process is characterized by the condition that $\sum_1 \Delta t^{(i)} = h$, where h is the time step size and the sum extends to all traversed segments.

3.4 Extension to Cyclic Loading Conditions

The model given in Eq. (2.1) is considered to be valid for metals at low homogeneous temperatures as long as $\sigma - G[\varepsilon]$ does not change sign [9]. In order to account for unloading beyond $\sigma = G[\varepsilon]$ one needs to modify the equation through introduction of new origins and updating of the viscosity function. The updating of the viscosity function is a recognition of the fact that the real material has changed its microstructure due to the loading up to the point $\sigma - G[\varepsilon] = 0$.

The stress update algorithm described above has been extended so as to be capable of treating unloading paths beyond $\sigma - G[\varepsilon] = 0$. This is achieved in a straightforward manner, by redefining the origin $0'$ (Fig. 1) of the stress-strain diagram along the (elastic) unloading path at a distance from point P_0 depending on the assumed hardening rule. Actually, Fig. 1 is a graphical representation of the equilibrium diagram updating during cyclic loading based on the illustrative assumption of isotropic hardening. It is further assumed that the time step size is sufficiently small that the equilibrium diagram segment between G_n and G_{n+1} is a straight line.

To illustrate the performance of the resulting algorithm, a simple calculation was performed for uniaxial cyclic loading at constant strain rate, $\dot{\varepsilon} = 1\ \mathrm{s}^{-1}$, using the fictitious material properties in [8, Table 2], and the assumption that the viscosity function does not require updating. The model response is shown in Fig. 2. Quasistatic and dynamic cyclic uniaxial experiments on stainless steel 316L are planned at JRC-Ispra in order to extend the calibration of the viscoplastic model to account for such loading conditions.

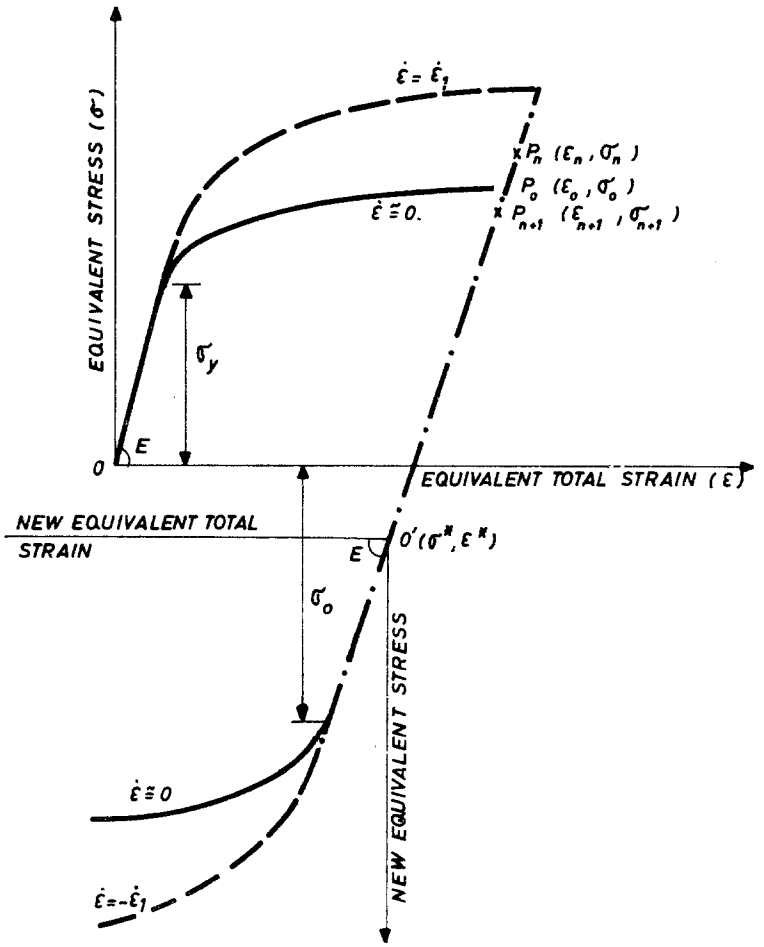

Fig. 1. Graphical representation of equilibrium diagram updating procedure during cyclic loading

The resulting algorithm is summarized in Table 1:

Table 1. *Stress update algorithm*

Step 1 Elastic predictor

$\boldsymbol{\sigma}_n$ and $\boldsymbol{\varepsilon}_n$ are given;

$\Delta\boldsymbol{\varepsilon} = h\dot{\boldsymbol{\varepsilon}}_{n+1/2}$ is prescribed (h = time step);

$\boldsymbol{\sigma}_{n+1}^{(0)} = \boldsymbol{\sigma}_n + \boldsymbol{D} \cdot \Delta\boldsymbol{\varepsilon}$;

$\boldsymbol{\varepsilon}_{n+1} = \boldsymbol{\varepsilon}_n + \Delta\boldsymbol{\varepsilon}$;

$\boldsymbol{G}_{n+1} = \boldsymbol{G}[\boldsymbol{\varepsilon}_{n+1}]$.

Table 1. (Fortsetzung)

Step 2 Check for overstress sign

$\sigma_{n+1}^{(0)} - G_{n+1} < 0$?

YES: $\varepsilon_0 = \varepsilon_n + (\varepsilon_n - \varepsilon_{n+1}) \cdot (G_n - \sigma_n)/(G_{n+1} - \sigma_{n+1})$

$\sigma_0 = G_{n+1} + (\varepsilon_0 - \varepsilon_{n+1}) \cdot (G_n - G_{n+1})/(\varepsilon_n - \varepsilon_{n+1})$

$\varepsilon^* = \varepsilon_0 - (2\sigma_0 - \sigma_y)/E$

$\sigma^* = \sigma_0 - \sigma_y$

(see notation in Fig. 1)

$\boldsymbol{\sigma}_{n+1} = \boldsymbol{\sigma}_{n+1}^{(0)}$

EXIT

NO: Go to step 3

Step 3 Check for inelastic behaviour

$\boldsymbol{Z}_{n+1}^{(0)} = \boldsymbol{\sigma}_{n+1}^{(0)} - \boldsymbol{G}_{n+1}$;

$\Gamma_{n+1}^{(0)} = \Gamma(\boldsymbol{Z}_{n+1}^{(0)})$

NO: EXIT

$\Gamma_{n+1}^{(0)} > 0$ YES: $i = 0$, $t^{(i)} = 0$.

Step 4 Plastic correctors

$$\bar{t}^{(i)} = \left[\frac{\eta}{1 - \dfrac{\partial \eta}{\partial \Gamma}\dfrac{\Gamma}{\eta}}\right]_{n+1}^{(i)}$$

$$\Delta\gamma = \frac{\Gamma_{n+1}^{(i)} \bar{t}^{(i)}}{\eta_{n+1}^{(i)}}$$

$$\boldsymbol{\sigma}_{n+1}^{(i+i)} = \boldsymbol{\sigma}_{n+1}^{(i)} - \Delta\gamma \left(\frac{d\Gamma}{d\boldsymbol{Z}}\right)_{n+1}^{(i)}$$

$$\boldsymbol{Z}_{n+1}^{(i+i)} = \boldsymbol{\sigma}_{n+1}^{(i+i)} - \boldsymbol{G}_{n+1}$$

$$\Gamma_{n+1}^{(i+i)} = \Gamma[\boldsymbol{Z}_{n+1}^{(i+i)}]$$

$$\Delta t^{(i)} = \bar{t}^{(i)} \log \left[\frac{(\Gamma/\eta)_{n+1}^{(i)}}{(\Gamma/\eta)_{n+1}^{(i+i)}}\right]$$

$$t^{(i+i)} = t^{(i)} + \Delta t^{(i)}$$

Step 5 Check for end of relaxation process

$t^{(i+i)} \geqq h$?

YES: $\Delta t^{(i)} = h - t^{(i)}$

$$\Delta\gamma = \frac{\Gamma_{n+1}^{(i)} \bar{t}^{(i)}}{\eta_{n+1}^{(i)}} [1 - \exp(-\Delta t^{(i)}/\bar{t}^{(i)})]$$

$$\boldsymbol{\sigma}_{n+1} = \boldsymbol{\sigma}_{n+1}^{(i)} - \Delta\gamma \left(\frac{d\Gamma}{d\boldsymbol{Z}}\right)_{n+1}^{(i)}$$

EXIT

NO: $i \to i + 1$; go to step 4.

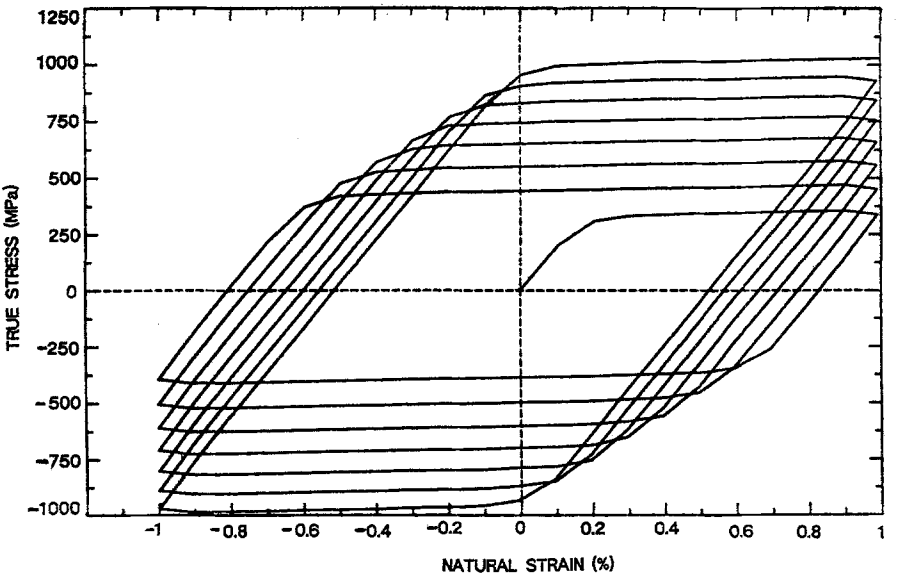

Fig. 2. Stress versus strain for cyclic loading under constant strain rate

4. Experimental Data

In this section we present the experimental data that were used to calibrate the viscoplastic model for both AISI 316L and AISI 316H.

4.1 Stainless Steel AISI Type 316L

A set of cylindrical specimens with dimensions as shown in Fig. 3 were prepared from AISI 316L stainless steel. The diameter tolerance was nominally ± 0.02 mm but was found to be ± 0.015 mm over the range of the samples tested.

The experiments were performed using a 400 kN Schenck servohydraulic testing machine operated in stroke displacement control. In order to obtain

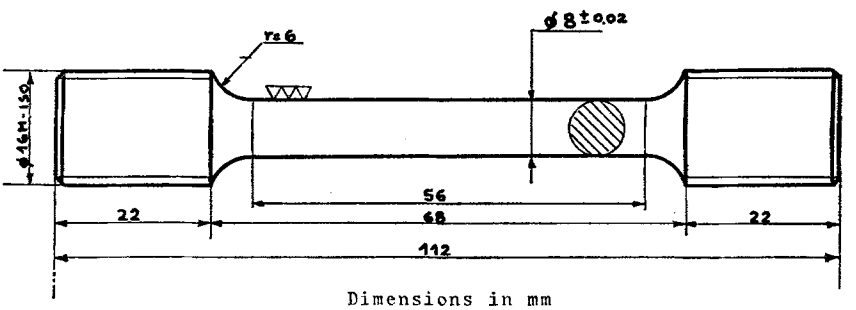

Fig. 3. Cylindrical specimen used in strain-rate tests for Stainless Steel type 316L

a constant stroke velocity, the displacement was continuously compared with a constant slope signal. Due to the fact that the specimen elongation V_s is equal to the stroke displacement X minus the deflection V_M arizing from the machine and specimen connections compliance, dV_s/dt is not constant. In order to overcome this inconvenience, without having to run the test under the more difficult conditions of strain control, the stroke reference signal X has been chosen as the sum of a linear input plus a fraction of the load signal. The appropriate choice of this fraction should compensate for the machine and specimen connection deflection so long as these remain proportional to the load.

The force was measured with a 63 kN load cell in series with the standard 400 kN device mounted on the machine. The strain was measured with an extensometer or strain gauges, depending upon the strain rate of the experiment. The extensometer strain measurement was used for strain rates up to $12 \times 10^{-3}\ s^{-1}$. For higher values, strain gauges were used in order to avoid extensometer damage and spurious measuring effects.

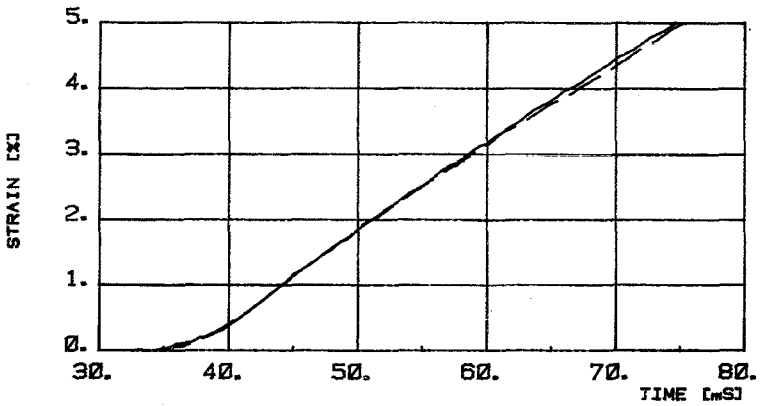

Fig. 4a. Comparison of the response of two strain gauges mounted on the same specimen

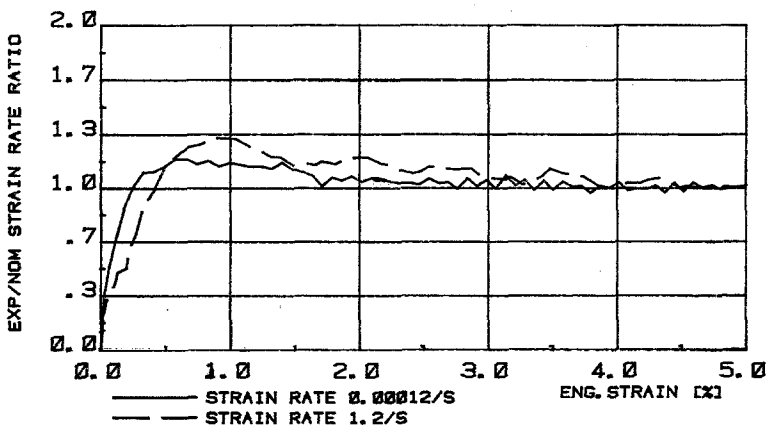

Fig. 4b. Experimental over nominal strain-rate ratio versus strain for two typical cases

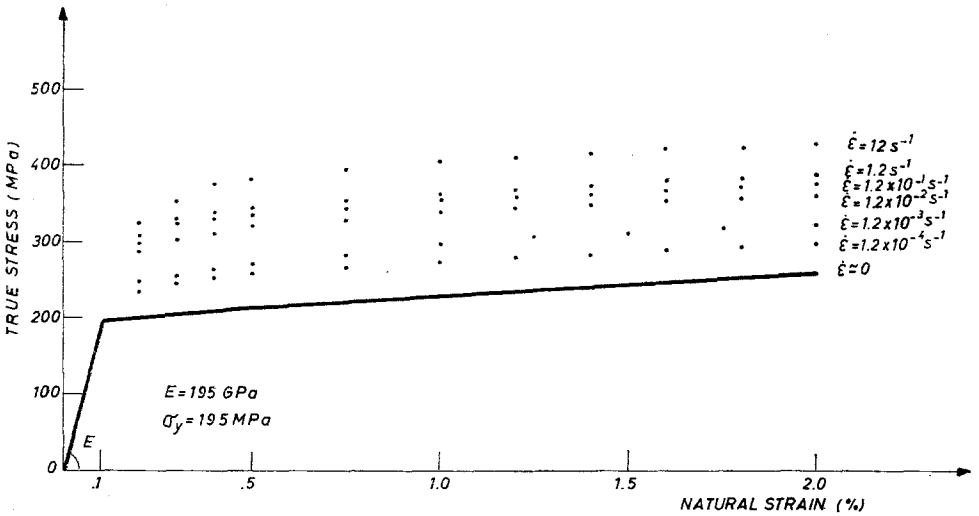

Fig. 5. Experimental data for stress versus strain at various strain rates for stainless steel type 316L including the postulated equilibrium diagram

A Hottinger Baldwin Messtechnik Linearly Variable Differential Transformer was used, having a range of ± 1 mm over a gauge length of 40 mm with a precision of $\pm 0.3\%$. The strain gauges, mounted on the specimen following a special procedure described in [10], can follow deformations of up to 20%. Two strain gauges were cemented axially at the centre of the specimen in diametral opposition.

Figure 4a compares the response of the two ganges at a strain rate of $1.2\ s^{-1}$. The overall deviation between the two signals is of the order of $\pm 2\%$.

Figure 4b shows two typical plots of strain rate versus strain. These were obtained by evaluating the ratio of the experimental to the nominal strain rate as set on the machine controls. The curves correspond to strain rates of 12×10^{-5} and $1.2\ s^{-1}$. It can be seen that after an initial transient (up to 1.5% engineering strain) the ratio is nearly unity. The maximum disparity between the experimental and nominal values is about 20% in the region of 0.5% engineering strain. Figure 5 shows the final experimental data for stress vs. strain at several constant strain rate values that were used for the calibration of the viscoplastic material model.

4.2 Stainless Steel AISI Type 316H

In order to calibrate the viscoplastic model and thereby predict the sensitivity to the rate of loading exhibited by AISI type 316H stainless steel, use is made of the experimental data obtained at room temperature using either Hopkinson bars or hydropneumatic loading devices depending on strain-rate level, as reported in [1]. Figure 6 shows the final experimental data for stress vs. strain at several constant strain rate values.

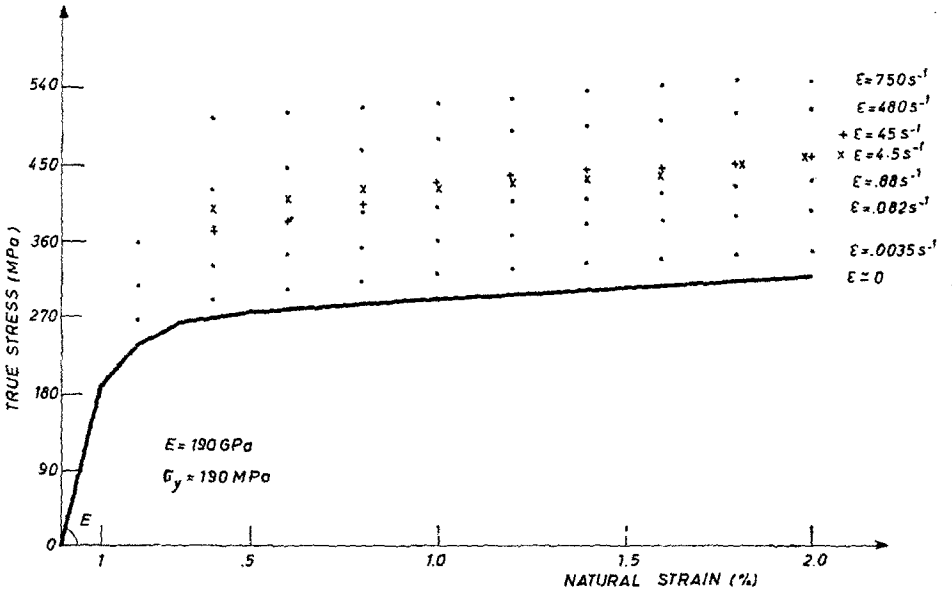

Fig. 6. Experimental data for stress versus strain at various strain rates for stainless steel type 316H including the postulated equilibrium diagram

5. Calibration of the Constitutive Model

Following [9], we assume that the viscosity function for both types of steel depends on the overstress magnitude as follows

$$\eta(\Gamma) = C_2 \exp\left\{C_3 \exp\left[-\left(\frac{\Gamma}{C_1}\right)^{C_4}\right]\right\} \tag{5.1}$$

where C_1, C_2, C_3 and C_4 are unknown material constants to be determined from experimental data.

It must be born in mind that in order to define completely the strain rate dependent material behaviour in monotonic loading, in addition to the viscosity constants on needs to know the equilibrium stress-strain diagram which of course cannot be obtained experimentally. For this reason such a diagram has been postulated based on the experimental results at the lowest strain rate available.

The procedure that was followed for the determination of the material constants in (5.1) is briefly summarized below. At first a parametric study was carried out that revealed the sensitivity of the model response (viscous part of stress at 2% strain) to each viscosity parameter separately, starting with the values in [8] for strain rate in the neighborhood of $\dot{\varepsilon} = 1\ s^{-1}$. These parameter values

are shown in Table 2 below

Table 2

$C_1 = 188.8$ MPa,	$C_2 = 0.2296 \times 10^{-6}$ s,	$C_3 = 28.19$,	$C_4 = 1.13$

This first step revealed that parameter C_3 in (5.1) should be considerably lower than originally assumed. After close examination of the results of the previous step, a parametric study was performed to determine the model sensitivity to the simultaneous variation of constants C_1 and C_2. It was concluded that by appropriate selection of values for this pair of parameters, one could maintain practically constant the model response in the 1% to 2% strain range and at the same time vary the deviation of the model response from the equilibrium diagram at strains below 1%.

It was conduded that for $C_1 = 1.888$ GPa and $C_2 = 0.2296 \times 10^{-8}$ s the numerical results were much closer to the experimental data available for both types of steel than was the case for the originally assumed values for this pair of parameters. Moreover this pair of values also seemed to yield a much more reasonable response for low values of strain rate (10^{-4}—10^{-2} s^{-1}). Upon further examination of the model response it was nevertheless concluded that the experimentally revealed material behaviour could not be simulated, to an acceptable degree of accuracy, in either case of stainless steel considered, unless one of the two remaining viscosity parameters (C_3 and C_4) is allowed to vary with strain rate. After extensive numerical experimentation, the selection of $C_4 = 1.25$ was made and C_3 was determined separately for the two different material types as described below.

5.1 Stainless Steel AISI Type 316L

Figure 5 shows experimental results of stress versus strain for the following values of strain rate: 1.2×10^{-4}, 1.2×10^{-3}, 1.2×10^{-2}, 1.2×10^{-1}, 1.2 and 12 s^{-1}.

The selected equilibrium diagram ($\dot{\varepsilon} = 0$) is also shown in the same figure. For the first trial it was taken into account that for $\dot{\varepsilon} = 3 \times 10^{-5}$ s^{-1} the viscous effect at 2% strain is about 7% for the present type of stainless steel [11].

It is clear from Fig. 5 that the spacing of the stress-strain diagrams in highly nonlinear. The stresses, at strain $\varepsilon = 2\%$ obtained with strain rates differing by several orders of magnitude are much less than one order of magnitude different. In fact, at strain $\varepsilon = 2\%$ and strain rate ratio $\dot{\varepsilon}_1/\dot{\varepsilon}_2 = 10^5$ one has a stress ratio $\sigma_1/\sigma_2 = 1.43 = 10^{0.155}$. Moreover, the stress value for $\dot{\varepsilon} = 1.2 \times 10^{-4}$ s^{-1} and at $\varepsilon = 2\%$ is about 15% higher than the "derived" equilibrium stress at that strain value. In addition, it is evident that the evolution of spacing of

the stress-strain diagrams, as the strain rate increases, does not exhibit any apparent regular pattern. Finally the stress-strain curves to a very good approximation have the same slope for strains higher than 1%.

As was stated before, the four viscosity parameters can not all be independent of strain rate. In fact we found that the material behaviour as shown in Fig. 5, is very well simulated in the strain rate range, $1.2 \times 10^{-4} - 1.2 \times 10^{1}\ s^{-1}$, by the following selection of values for the viscosity function parameters:

$$C_1 = 1.888\ \text{GPa}; \qquad C_2 = 0.2296 \times 10^{-8}; \qquad C_4 = 1.25 \tag{5.2}$$

while C_3 is strain-rate dependent as Table 3 below indicates.

Table 3. *C_3 versus $\dot{\varepsilon}$ for 316L*

$\dot{\varepsilon}$:	.00012	.0012	.012	.12	1.2	12	(s^{-1})
C_3:	20.7	19.0	17.28	15.1	12.9	10.9	

Figure 7 shows that C_3 is to a good approximation linear in $\ln \dot{\varepsilon}$, i.e.,

$$C_3 = 13.07 - 0.903 \ln \dot{\varepsilon}. \tag{5.3}$$

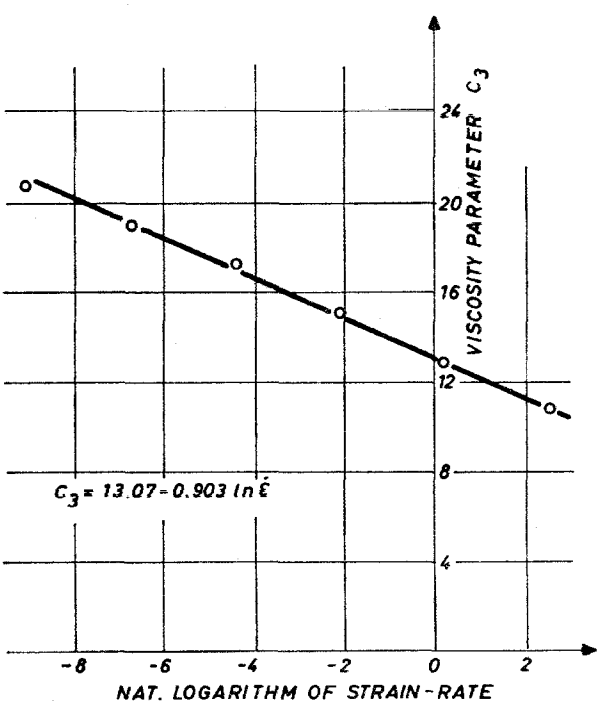

Fig. 7. Viscosity function coefficient C_3 versus $\ln \dot{\varepsilon}$ for stainless steel type 316L

Figures 8 and 9 show numerical results at constant strain rates using the values of Table 3 and Eq. (5.3) respectively, while Fig. 10 shows a comparison of the numerical results of Fig. 8 with the experimental data.

Thus it is concluded that in the strain rate range of $10^{-4}\,s^{-1}$ to $10\,s^{-1}$ and for deformations up to 2%, the viscoplastic behaviour of stainless steel AISI

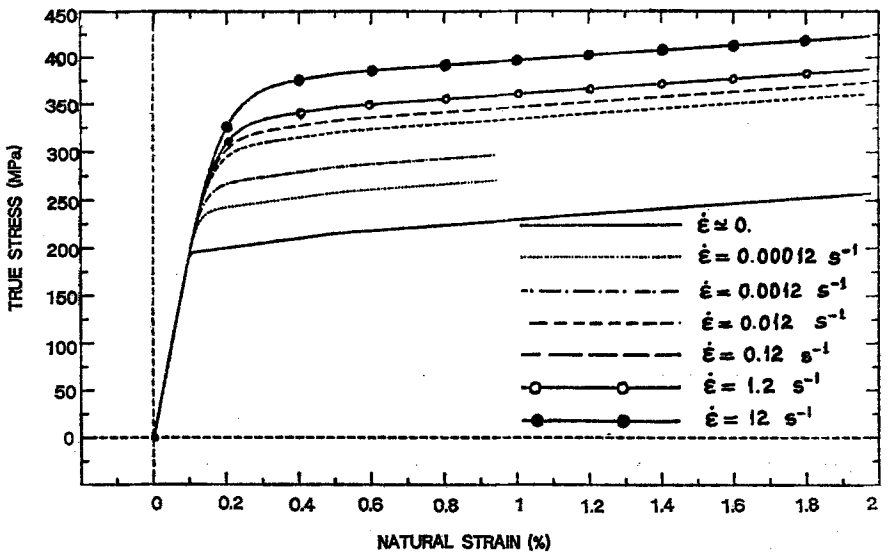

Fig. 8. Numerical results for stress versus strain for stainless steel 316L using Table 3

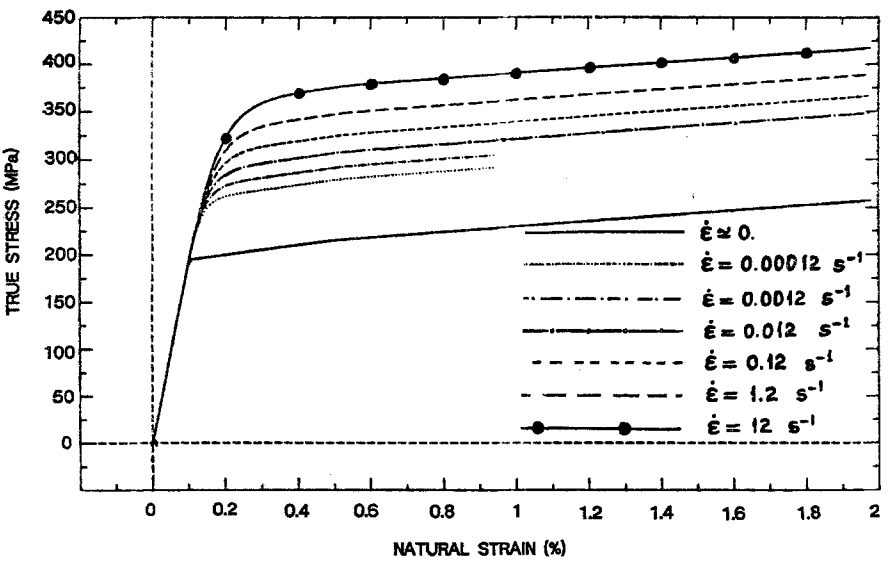

Fig. 9. Numerical results for stress versus strain for stainless steel 316L using Eq. 5.3

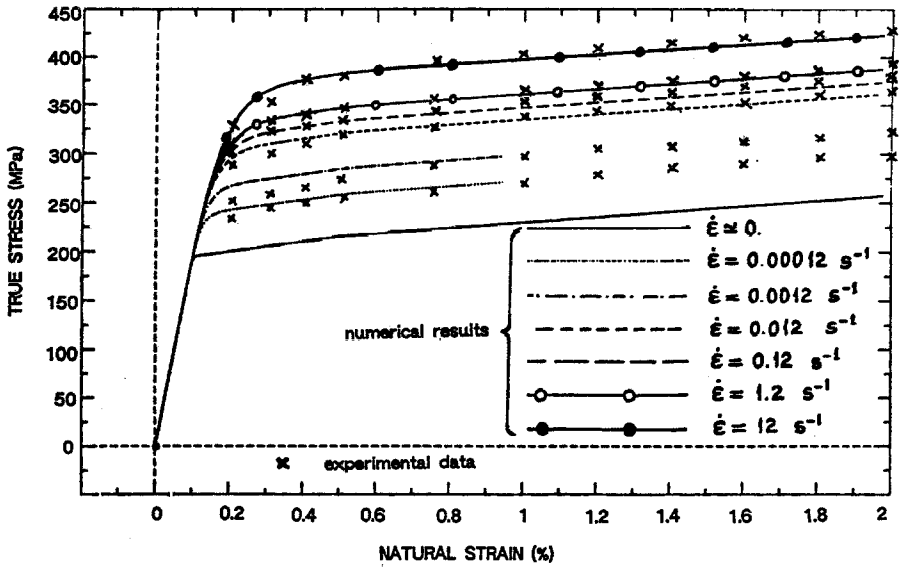

Fig. 10. Numerical (using Table 3) and experimental results for stress versus strain for stainless steel 316L

type 316L is described with an excellent approximation by the constitutive Eqs. (2.1) through (2.6), the viscosity function (5.1) and the material properties given in Table 4.

Table 4. *Material properties of AISI 316L Stainless Steel*

1. *Viscosity function coefficients*	
$C_1 = 1.888$ GPa, $C_2 = 0.2296 \times 10^{-8}$ s, $C_4 = 1.25$ and $C_3 = 13.07 - 0.903 \ln \varepsilon$	
2. *Equilibrium stress-strain diagram*	
Elastic Modulus:	195 GPa
First yield stress:	195 MPa
First hardening slope:	5.25 GPa
Second yield stress:	216 MPa
Second hardening slope:	2.93 GPa
3. *Other properties*	
Density:	8000 kg/m^3
Poisson's ratio:	0.3

5.2 Stainless Steel AISI Type 316H

Figure 6 shows experimental results for stress versus strain for the following values of strain rate:

$$.0035,\ .082,\ .88,\ 4.5,\ 45,\ 480 \text{ and } 750\ s^{-1}$$

The selected equilibrium diagram ($\dot{\varepsilon} = 0$) is also included in the same figure.

Here again one observes that the spacing of the stress-strain diagrams is highly nonlinear and to a good approximation they have the same slope for strains higher than 1%. However, in this case one also observes that for strain rates 4.5 s^{-1} and 45 s^{-1} and in the strain range of 1% to 2% the stresses are practically coincident. Of course, one could compare this experimental phenomenon with that of the thinly spaced response exhibited by 316L in the strain rate neighborhood of 1.2×10^{-2} to 1.2 s^{-1}. Such a comparison, however, is probably of limited value because of lack of experimental data at strain rates higher than 12 s^{-1} in the case of AISI 316L.

The values in Table 5 for the viscosity function coefficient C_3 and the values given in (5.2) for the remaining constants yield an excellent agreement between the experimental and numerical data in the range of strain rate of 4.5 s^{-1} to 750 s^{-1}.

Table 5. *C_3 versus $\dot{\varepsilon}$ for 316H*

$\dot{\varepsilon}$:	4.5	45.	480	750	(s^{-1})
C_3:	11.5	9.15	7.30	7.00	

Figure 11 shows that parameter C_3 is parabolic in $\ln \dot{\varepsilon}$. In fact, from the first three values of Table 5 one obtains:

$$C_3 = 13.32 - 1.29 \ln \dot{\varepsilon} + .05 (\ln \dot{\varepsilon})^2 \tag{5.4}$$

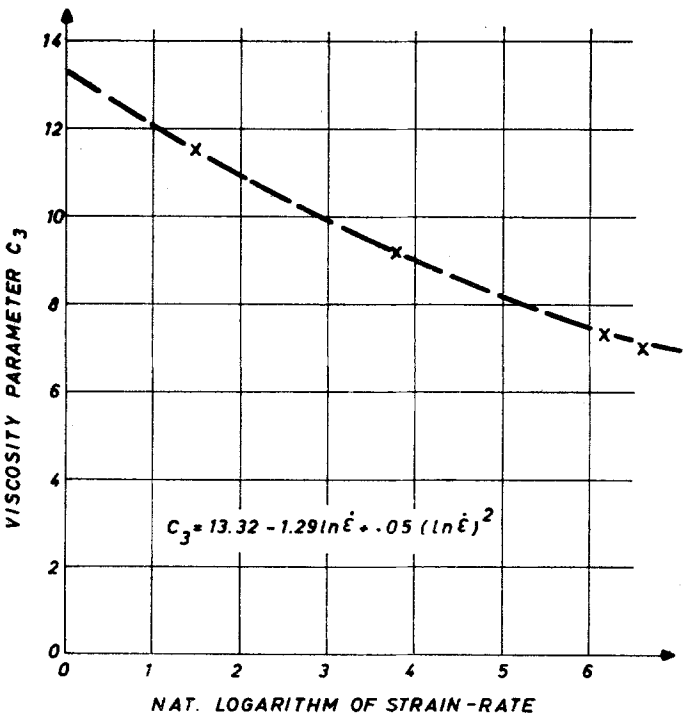

Fig. 11. Viscosity function coefficient C_3 versus $\ln \dot{\varepsilon}$ for stainless steel type 316H

Substituting in (5.4) for $\dot{\varepsilon} = 750\ s^{-1}$ one finds

$$C_3|_{\dot{\varepsilon}=750s^{-1}} = 6.97,$$

which is within 1% of the estimated value of 7.0 from the numerical model.

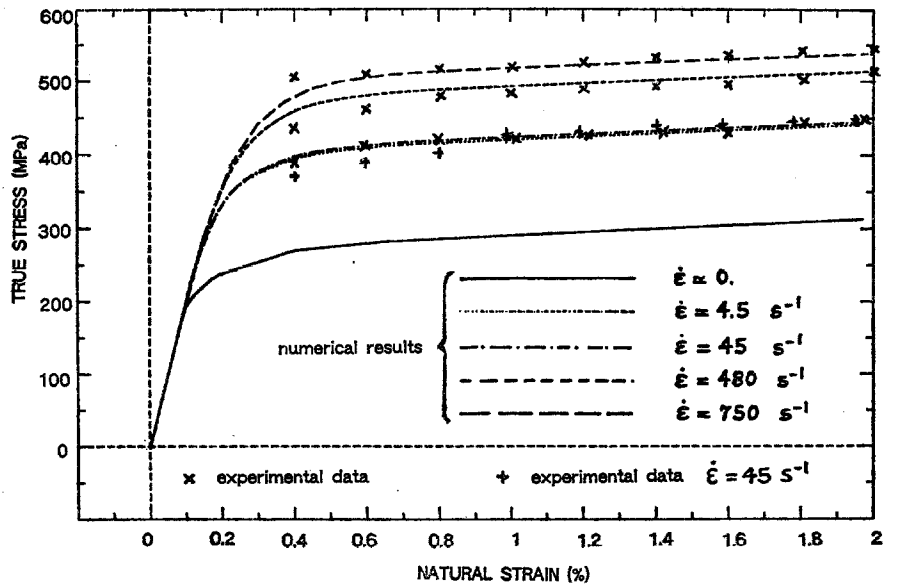

Fig. 12. Numerical and experimental results for stress versus strain for stainless steel 316H

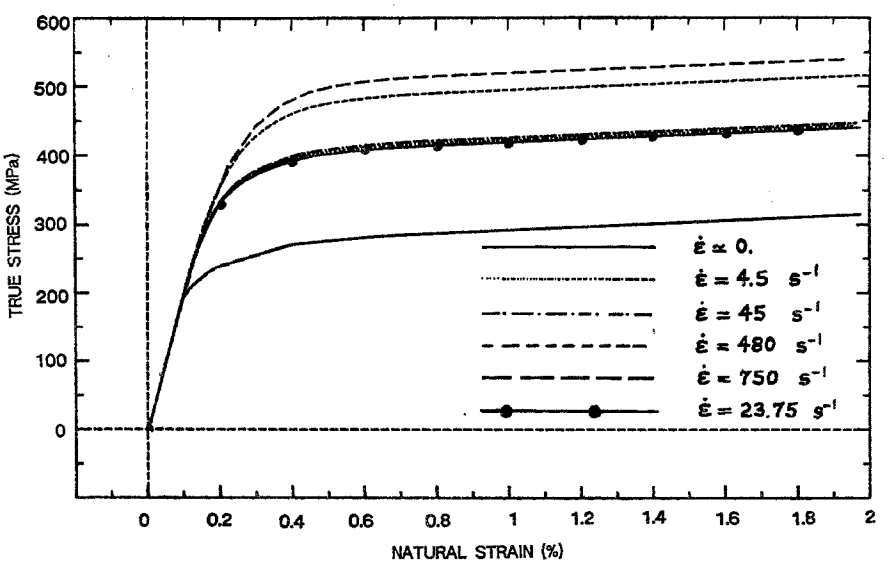

Fig. 13. Numerical results for stress versus strain for stainless steel 316H showing performance of the model in the strain-rate range of 4.5 to 45 s^{-1}

Figure 12 shows an excellent agreement between experimental data and numerical results.

Another indication that the parabolic relation (5.4) is adequate is the fact that the numerical model response for a randomly selected value of strain rate in between the experimental values 4.5 and 45 s^{-1}, i.e., $\dot{\varepsilon} = 23.75\ s^{-1}$, coincides with the experimental observations (Fig. 13).

6. Numerical Examples

The calibrated viscoplastic material model and the related stress-update algorithm described in Section 3 have been incorporated into the transient dynamic Computer Code PLEXIS-3C jointly developed by CEA (CEN-Saclay) and CEC (JRC-Ispra). The resulting subroutine has been linked to several two- and three-dimensional finite elements available in the PLEXIS library.

In order to illustrate the significant effect of the rate of loading on the stress distribution, two numerical examples will be presented using the material properties reported in Table 4 for the nonlinear viscoplastic behaviour of stainless steel AISI 316L. For comparison purposes, numerical results have also been derived for the case of linear viscosity ($\eta = C_2$) and for inviscid plasticity.

6.1 Thick-Walled Cylinder Under Internal Pressure

The first example considers a thick-walled cylinder with axially fixed ends submitted to internal pressure. The cylinder has an outer to inner radius ratio of 2, and is modelled using 9-node Lagrange finite elements as shown in Fig. 14. The loading rate is taken 1 GPa s^{-1} and the maximum applied pressure is 280 MPa.

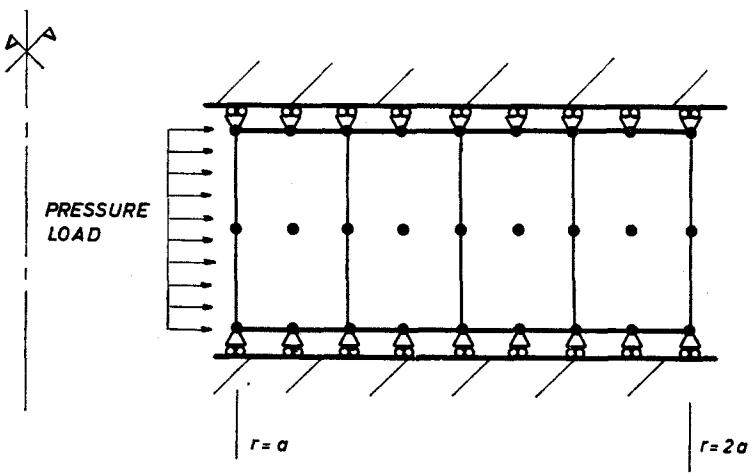

Fig. 14. Finite element model for internally pressurized cylinder

This loading rate corresponds to a strain rate in the range 10^{-2}—10^{-1} s^{-1} at the inner surface of the cylinder.

Figures 15a and 16a show hoop and equivalent stresses, respectively, versus internal pressure, while in Figs. 15b and 16b similar results are shown for purely elastoplastic material behaviour. The comparison of the numerical results shown in Figs. 15a and 15b on one hand and those in Figs. 16a and 16b on the other

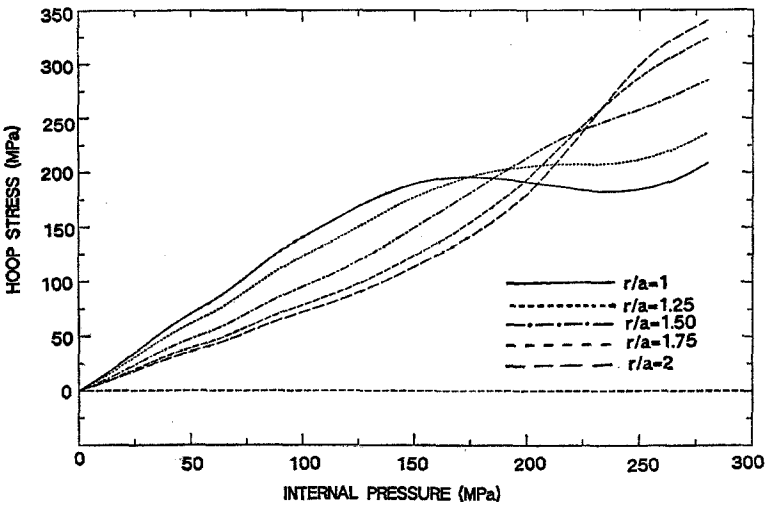

Fig. 15a. Hoop stress versus internal pressure at various r/a ratios based on the calibrated model for stainless steel type 316L

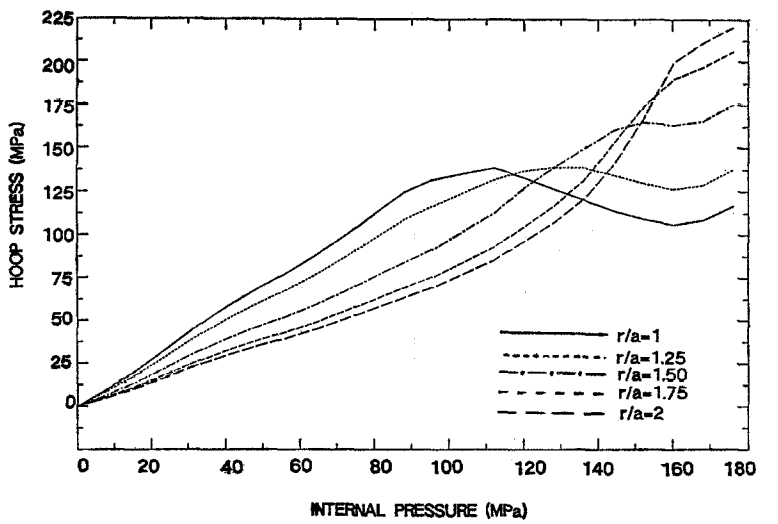

Fig. 15b. Hoop stress versus internal pressure at various r/a ratios assuming simple elastoplastic behaviour for stainless steel type 316L

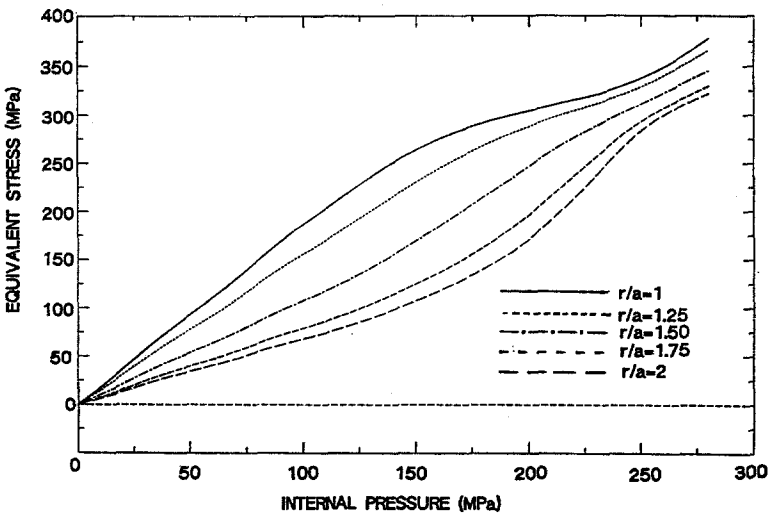

Fig. 16a. Equivalent stress versus internal pressure at various r/a ratios based on the calibrated model for stainless steel type 316L

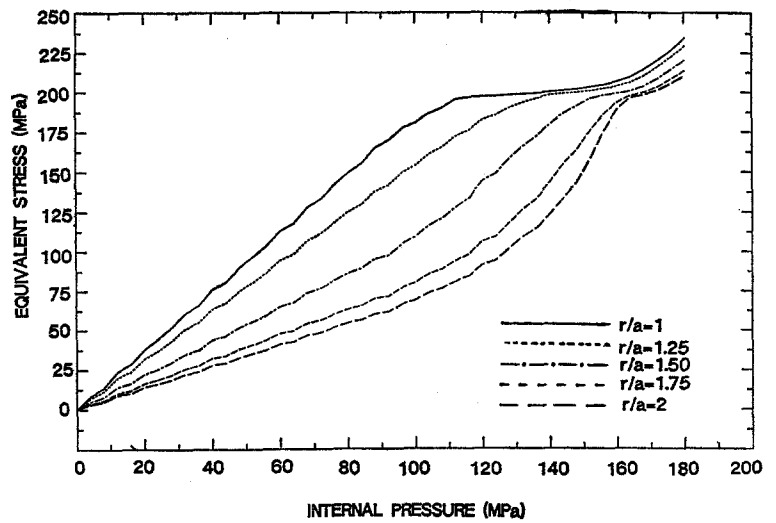

Fig. 16b. Equivalent stress versus internal pressure at various r/a ratios assuming simple elastoplastic behaviour for stainless steel type 316L

hand illustrate the significant effect of the viscoplastic behaviour on the structural response even at such moderate strain rates.

More specifically, for the viscoplastic material law the hoop stress at the inner surface of the cylinder increases practically linearly up to about 180 MPa, which corresponds to an internal pressure of 130 MPa, while for the purely elastoplastic law significant deviation from linearity begins at 125 MPa which corresponds to an internal pressure of 90 MPa. Maximum hoop stress at the inner

surface in the viscoplastic case is by about 40% higher than that for the elastoplastic case. In the elastoplastic case the equivalent stress near the inner surface increases linearly until the yield stress is reached and hardening does not commence there until the yield stress is reached throughout the cylinder, thus leading to an ideally plastic behaviour in the mean time. Contrary to the above is the viscoplastic case where the viscous effect yields a hardening effect throughout the material in a continuous manner following the original linear response.

6.2 Thin-Walled Vessel Under Internal Pressure

A thin-walled vessel under high internal pressure rate is now considered. The finite element model of the vessel is shown on Fig. 17 and consists of 11 conical shell elements based on Kirchhoff theory. Four different loading rates were analyzed: 50, 500 and 5000 GPa s^{-1} where the radius to thickness ratio was taken to be 6.25 (cases *A*, *B* and *C*) and finally 50000 GPa s^{-1} where that ratio was taken to be 12.5 (case *D*). Thus it was possible to study the structural response that corresponds to strain rates of $3 \div 30\ s^{-1}$ for the *A*, *B* and *C* cases and around $150\ s^{-1}$ for case *D*. All transient analyses performed were run up to the point where the mean equivalent strain reached the value of one percent.

Numerical results are presented for equivalent stress vs. internal pressure. For pressure rates of 50 and 500 GPa s^{-1} (Figs. 18 and 19) two material behaviour cases are shown for comparison purposes (elastoplastic and nonlinear viscoplastic). Finally for pressure rate of 5000 and 50000 GPa s^{-1} (Figs. 20 and 21), three material behaviour cases are shown (nonlinear viscoplastic ($\eta = \eta(\Gamma)$), linear viscoplastic ($\eta = C_2$) and purely elastoplastic).

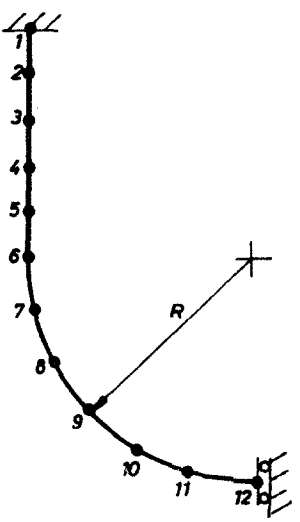

Fig. 17. Finite element model for pressurized vessel

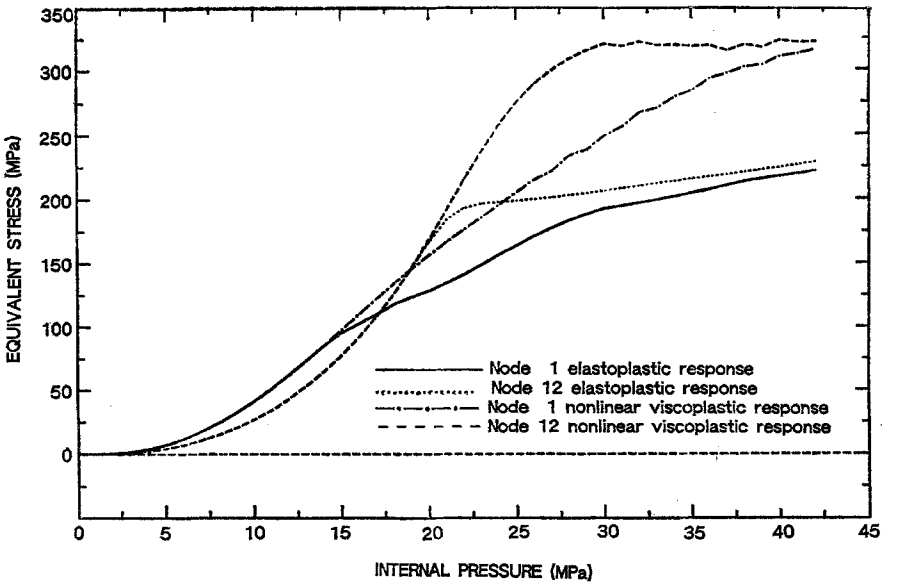

Fig. 18. Equivalent stress versus internal pressure for $\dot{P} = 50$ GPa s^{-1} at nodes 1 and 12 of the pressure vessel and for elastoplastic and viscoplastic behaviour of stainless steel type 316L

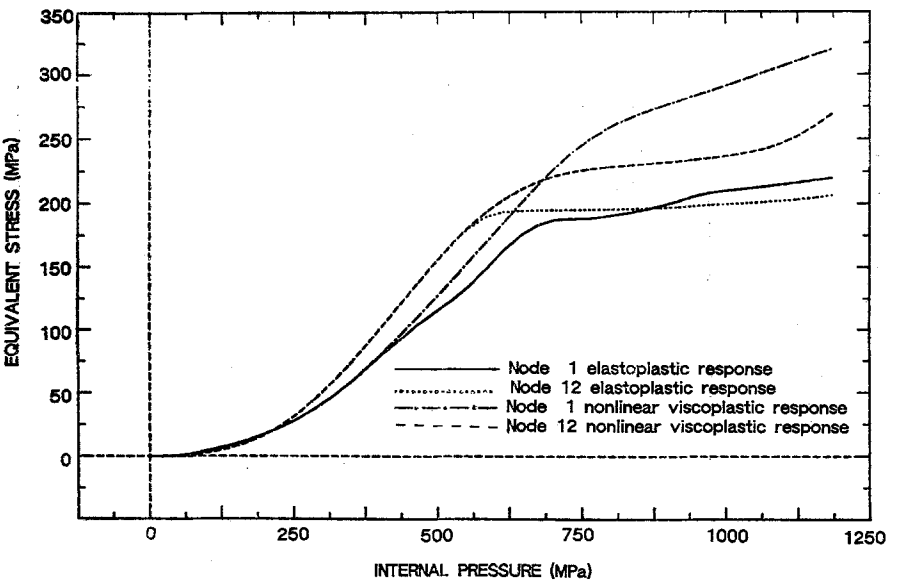

Fig. 19. Equivalent stress versus internal pressure for $\dot{P} = 500$ GPa s^{-1} at nodes 1 and 12 of pressure vessel and for elastoplastic and viscoplastic behaviour of stainless steel type 316L

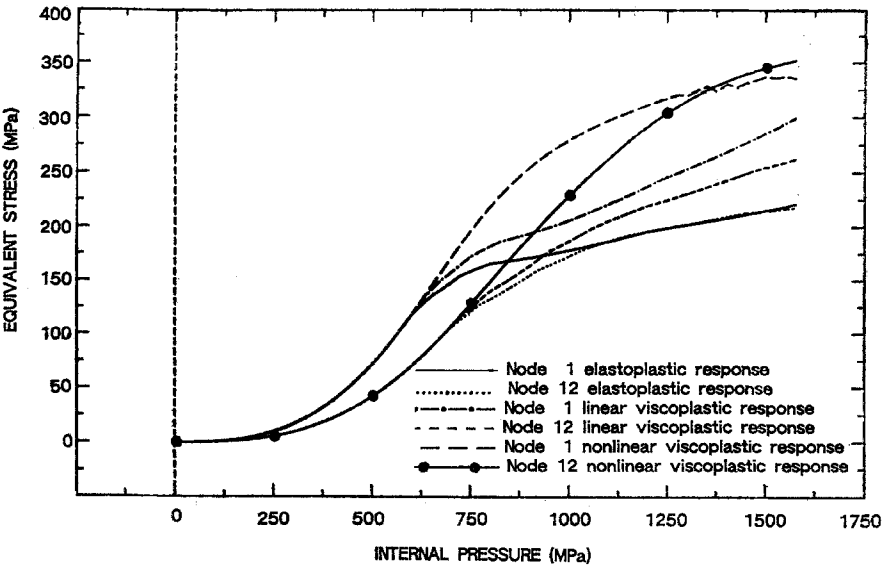

Fig. 20. Equivalent stress versus internal pressure for $\dot{P} = 5000\,\mathrm{GPa\,s^{-1}}$ at nodes 1 and 12 of pressure vessel and for elastoplastic and viscoplastic behaviour of stainless steel type 316L

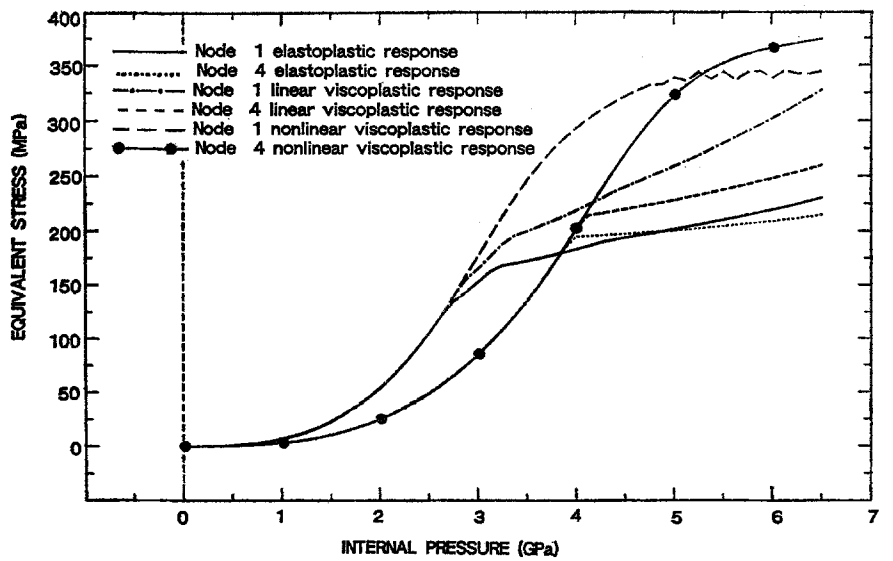

Fig. 21a. Equivalent stress versus internal pressure for $\dot{P} = 50000\,\mathrm{GPa\,s^{-1}}$ at nodes 1 and 4 of pressure vessel and for 3 material laws for 316L stainless steel

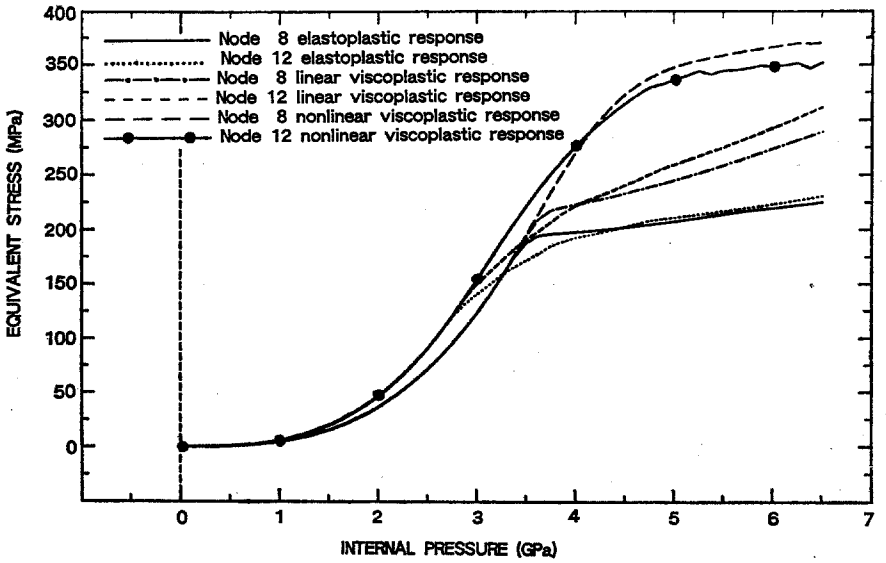

Fig. 21b. Equivalent stress versus internal pressure for $\dot{P} = 50000$ GPa s^{-1} at nodes 8 and 12 of pressure vessel and for 3 material laws for 316L stainless steel

As could be seen from the numerical results for the two lower pressure rates, the deformation histories vary after yield stress is reached depending on whether the viscosity function is constant or depends on the overstress. Contrary to this, for the two higher pressure rates the deformation history throughout the vessel is practically the same. However, as also shown in Figs. 20 and 21, the stress results for linear and nonlinear viscoplastic material behaviour are different for these two higher loading rate cases.

From the plotted results for equivalent stress one observes that the nonlinear viscoplastic behaviour response at the end of the transient is higher than that of the simple elastoplastic behaviour by about 40%—65% as pressure rate increases. In addition, as expected, the response due to linear viscoplastic behaviour falls in between the other two. Finally for the two extreme pressure-rate cases, 50 and 50000 GPa s^{-1}, which yield strain rates of 3 and 150 s^{-1}, respectively, the equivalent stress response at the end of the transient differs by about 15% as Table 6 indicates.

Table 6

Node No.	Equivalent stress ($\dot{P} = 50$ GPa s^{-1})	Equivalent stress ($\dot{P} = 50000$ GPa s^{-1})
1	316 MPa	346 MPa
12	323 MPa	353 MPa

7. Conclusions

The viscoplastic constitutive model developed by Cernocky and Krempl has been implemented in a transient finite element code together with an efficient stress update algorithm based on the elastic predictor-return mapping concept. The model has been calibrated to reproduce the uniaxial response of both stainless steels AISI 316L and 316H and applied to predict the response to transient loading of two representative structures.

However, the performance of the model needs to be further examined in comparison with two-dimensional strain rate experimental data and its calibration must be extended to account for cyclic loading cases. Therefore, further experimental work is required in uniaxial cyclic quasistatic and dynamic loading, as well as in two-dimensional monotonic loading.

References

[1] Albertini, C., Cenerini, R., Curioni, S., Montagnani, M.: Dynamic mechanical properties of austenitic stainless steels-fitting of experimental data on constitutive equations. VII SMIRT, August 1983, Chicago, paper L 2/4 53—62.

[2] Malvern, L. E.: The propagation of longitudinal waves of plastic deformation in a bar of material exhibiting a strain rate effect. Trans. ASME 73, Ser. E, J. Appl. Mech. **18**, 203—208 (1951).

[3] Perzyna, P.: The constitutive equations for rate sensitive plastic materials. Q. Appl. Math. **20**, 321—332 (1963).

[4] Bodner, S. R., Partom, Y.: Constitutive equations for elastic-viscoplastic strain hardening materials. J. Appl. Mech. **42**, 2, 385—389 (1975).

[5] Cernocky, E. P., Krempl, E.: A theory of viscoplasticity based on infinitesimal total strain. Acta Mechanica **36**, 263—289 (1980).

[6] Simo, J. C., Ortiz, M.: A unified approach to finite deformation elastoplastic analysis based on the use of hyperelastic constitutive equations. Comput. Meths. Appl. Mech. Engrg. **49**, 221—245 (1985).

[7] Hughes, T. J. R.: Numerical implementation of constitutive models: rate-independent deviatoric plasticity. In: Theoretical foundation for large-scale computations of nonlinear material behaviour (Nemat-Nasser, S. et al., eds.), pp. 29—63. Martinus Nijhoff Publishers 1984.

[8] Donea, J., Youtsos, A. G., Casadei, F.: A stress update algorithm for the theory of viscoplasticity based on total strain and overstress. Proceedings of the International Conference on Computational Plasticity, Models, Software and Applications, Barcelona, Spain, April 6—10, 1987, pp. 413—424. Pineridge Press 1987.

[9] Liu, M. C. M., Krempl, E.: A uniaxial viscoplastic model based on total strain and overstress. J. Mech. Phys. Solids **27**, 377—391 (1979).

[10] Casadei, F., Delzano, C., Magonette, G., Halleux, J. P., Verzeletti, G.: Dynamic testing of large AISI-316L steel specimens behaviour using LDTF. Nucl. Eng. Design **102**, 463—474 (1987).

[11] Han, S.: Le comportement d'hystérésis des solides et sa description par un schéma à mémoire discrète. Thèse présentée à l'Institut National Polytechnique de Grenoble, 1985.

A. G. Youtsos, J. Donea, and G. Verzeletti
Applied Mechanics Division
Joint Research Centre of the Commission
of the European Communities
I-21020 Ispra (VA)
Italy